Scientific Research Publishing

Journal of Power and Energy Engineering, 2025, 13(9), 343-370
https://www.scirp.org/journal/jpee
ISSN Online: 2327-5901
ISSN Print: 2327-588X

Design and Development of Wi-Fi and GPS-Based Smart Monitoring and Fault Detection System for Three-Phase Power Transmission Line Using Arduino

Sarweash Rao Tharma Raja[1], Mohd Firdaus Mohd Ab Halim[1*], Syed Muhammad Naufal Syed Othman[2], Mohd Hafiz Bin Jali[1]

[1]Faculty of Electrical Technology and Engineering (FTKE), Universiti Teknikal Malaysia Melaka (UTeM), Melaka, Malaysia
[2]Faculty of Electrical and Electronic Engineering (FKEE), Universiti Tun Hussein Onn Malaysia (UTHM), Batu Pahat, Malaysia
Email: *mohd.firdaus@utem.edu.my

How to cite this paper: Raja, S.R.T., Ab Halim, M.F.M., Othman, S.M.N.S. and Jali, M.H.B. (2025) Design and Development of Wi-Fi and GPS-Based Smart Monitoring and Fault Detection System for Three-Phase Power Transmission Line Using Arduino. *Journal of Power and Energy Engineering*, **13**, 343-370.
https://doi.org/10.4236/jpee.2025.139023

Received: July 23, 2025
Accepted: September 21, 2025
Published: September 24, 2025

Abstract

Rapid and accurate detection, classification, and localization (DCL) of faults in overhead transmission lines (TLs) are critical for minimizing downtime and enhancing power system resilience, particularly as these lines often traverse remote and environmentally vulnerable regions. This paper proposes an Internet of Things (IoT)-based intelligent monitoring system for real-time fault DCL in TLs. A hardware prototype was developed using a scaled single-phase, four-wire configuration to emulate three-phase behaviour. The system integrates an Arduino Mega for sensor data acquisition, an ESP32 module for wireless communication, and a NEO-6MV GPS module for geographic localization. Real-time current readings are captured via ACS712 sensors and transmitted to the Arduino IoT Cloud platform for remote monitoring. The system also delivers live fault alerts, specifying fault type, affected phase, and exact location, to the responsible engineer and load dispatch centre via cloud-based notifications. The prototype successfully identified 24 different fault scenarios, including single-line-to-ground (SLG) and double-line-to-ground (DLG) faults across four distinct zones, demonstrating 100% detection, classification, and localization accuracy over 960 trials. This work represents a scalable and cost-effective solution for innovative TL fault management and lays the groundwork for real-time fault analysis systems in modern power grids.

Keywords

Internet of Things (IoT), Smart Grid, Transmission Line Fault Detection, Arduino, GPS Localization, Power System Reliability

1. Introduction

Electrical power systems form the backbone of modern infrastructure and are typically divided into three main stages: generation, transmission, and distribution. Power plants convert primary energy sources into electricity, which is transported over long distances through high-voltage transmission lines before being stepped down and delivered to consumers via distribution networks. The transmission system is the backbone of these stages, ensuring bulk power delivery across regions. However, because of their vast geographical exposure and operational stress, transmission lines (TLs) remain particularly vulnerable to faults, making their monitoring and protection crucial for reliable operation [1].

As a cornerstone of national critical infrastructure, the smart grid has emerged as a focal point of innovation across governmental, industrial, and academic sectors [2]. Central to its functionality is deploying an advanced monitoring system that oversees and manages grid operations, enabling optimized control, protection, and resilience. These systems provide real-time visualization of network conditions, which supports informed decision-making and rapid fault response [3]. A primary objective of such monitoring systems is to minimize outage durations caused by faults and thereby enhance the continuity of supply [4] [5].

Faults in TLs compromise system stability and reliability and result in costly outages and safety risks. Locating the exact fault position across an expansive network remains a labour-intensive and time-consuming task [6] [7]. In many instances, utilities are forced to shut down entire grid sections simply to trace the fault location, leading to prolonged disruptions and economic losses [8]. This underscores the urgent need for efficient, automated fault detection, classification, and localization (DCL) techniques that can operate in real time.

Fault Classification in Transmission Line

Faults in TLs can be broadly classified into transient and intransient (permanent) types [9], as illustrated in **Figure 1**. Transient faults are typically short-lived and self-clearing, often caused by external environmental conditions such as temporary contact with trees, animal interference, lightning, or conductor clashes during storms. Although transient, these faults can trigger severe operational disturbances if not promptly managed.

Intransient faults, however, are permanent and require corrective action. They are further subdivided into open-circuit faults and short-circuit faults. Open-circuit faults involve one or more broken phases that interrupt current flow. Short-circuit faults are more critical and can be categorized into phase and ground faults.

- Phase faults occur when two or more phases short-circuit. These can be symmetrical (LLL, involving all three phases, the most severe but least common fault) or asymmetrical (LL, line-to-line faults).
- Ground faults occur when one or more phases come into contact with the ground, and are more frequent in distribution systems. They are classified as:

  1) LG/SLG—(Single Line-to-Ground),

2) LLG/DLG—(Double Line-to-Ground),
3) LLLG—(Triple Line-to-Ground).

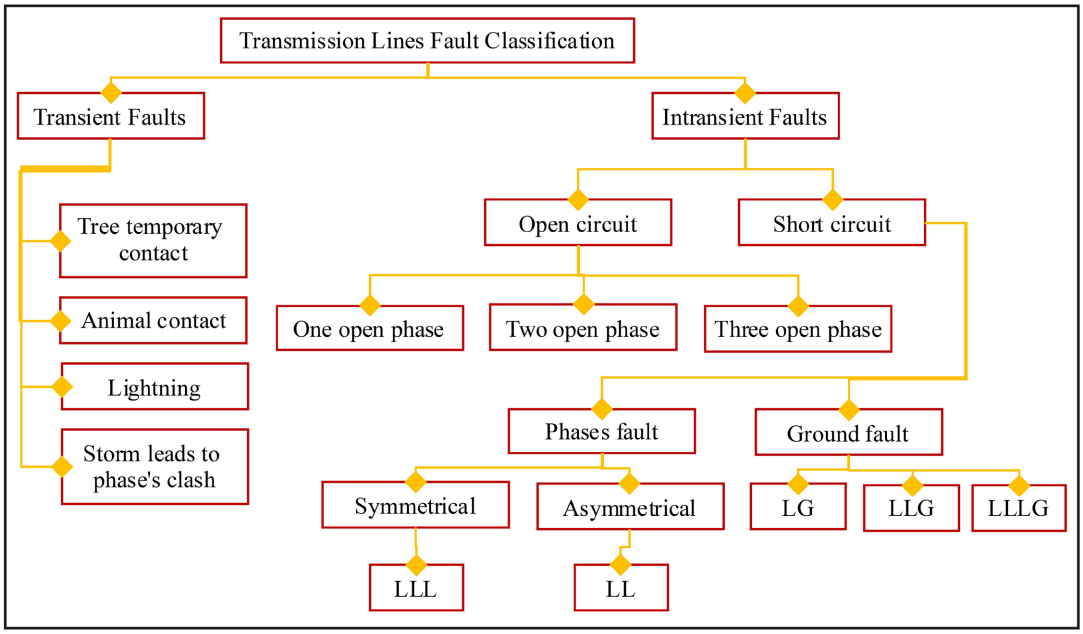

Figure 1. Hierarchical classification of faults in transmission lines showing transient and intransient fault types, including open circuits, short circuits, phase, and ground-related faults [9].

Over the years, extensive research has focused on developing high-efficiency fault diagnosis techniques, with early and accurate detection being critical for ensuring system reliability and minimizing damage [10]. An effective detection system must therefore not only distinguish between transient and permanent faults but also provide real-time fault type identification and precise localization. This growing demand highlights the importance of integrating IoT, GPS, and Wi-Fi-based technologies into modern TLs' monitoring and protection schemes.

2. Literature Review

The increasing complexity of power transmission networks, particularly in extra high voltage (EHV) and ultra-high voltage (UHV) systems, necessitates rapid and precise fault detection, classification, and localization (DCL) to minimize downtime and enhance grid resilience. Conventional fault detection methods, such as impedance-based relays and manual inspections, often suffer from limited accuracy and response delays, particularly in remote or environmentally vulnerable regions. To address these challenges, recent advancements in Internet of Things (IoT) and microcontroller-based monitoring systems have introduced cost-effective, real-time solutions for fault management.

2.1. Advancements in IoT-Based Fault Detection for Transmission Lines

Several researchers have explored Arduino-based systems with varying degrees of

sophistication. For example, [11] implemented an Arduino UNO with resistive fault simulations to detect line-to-line (LL) faults, with fault information displayed on an LCD. While low-cost and straightforward, this approach lacked remote monitoring capability and relied on manual fault induction, limiting its practical use in real transmission networks.

To improve real-time communication, [12] and [7] integrated GSM modules for SMS-based fault alerts. Alam's system further incorporated GPS functionality for fault localization, which enhances field response efficiency. However, these solutions remained dependent on cellular networks, which may be unreliable in remote areas. Moreover, their fault classification relied only on basic voltage and current thresholds, without incorporating repeated testing across multiple cycles to validate the robustness and consistency of the fault management system.

In parallel, [13] introduced an Artificial Neural Network (ANN)-based approach for fault DCL in mesh networks, achieving high precision. While highly accurate and effective, ANN methods require large datasets and significant computational resources, making them less feasible for low-cost deployments. Addressing modularity, [14] combined Arduino UNO with ESP32 IoT connectivity, using the Twilio API for SMS alerts. Their system demonstrated scalability but lacked GPS-based localization, a critical feature for rapid field deployment. Similarly, [15] and [16] propose prototype-based solutions, emphasizing affordability and real-time performance. Yet, these prototypes did not include advanced IoT features such as cloud-based data logging or geospatial tracking, which are essential in modern innovative grid applications.

2.2. Research Gaps and Motivations

Despite these advancements, existing fault management solutions exhibit several limitations regarding scalability, cloud integration, and precise localization. Most systems cannot handle large-scale grid applications, real-time cloud data logging and visualization are often absent, and GPS-based, meter-level fault pinpointing is rarely included.

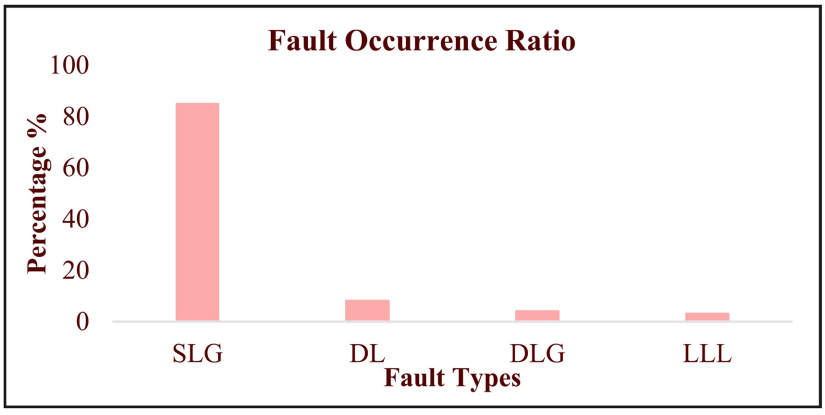

Figure 2. Fault occurrence ratio in transmission line.

Furthermore, research indicates that ground faults such as single line to ground (SLG) faults account for nearly 80% of transmission line failures in extra high voltage (EHV) and ultra-high voltage (UHV) systems [17]-[19], as shown in **Figure 2**. The inclusion of double line-to-ground (DLG) fault detection is equally crucial from a safety perspective. A ground fault creates dangerous voltage potential differences in the surrounding terrain, necessitating wider area evacuation protocols during maintenance. While three-phase-to-ground (LLLG) faults are more severe, SLG and DLG faults occur more frequently and are thus the primary focus of current research.

2.3. Contribution of This Work

To address these gaps, this paper proposes an innovative IoT-based smart monitoring system for comprehensive transmission line fault detection, classification, and localization (DCL). The system integrates ACS712 current sensors for accurate current monitoring, an Arduino Mega microcontroller for real-time data acquisition and processing, an ESP32 Wi-Fi module for cloud connectivity, and a NEO-6MV GPS module for meter-level geolocation of faults.

This integrated approach enhances fault localization accuracy, reducing system downtime and maintenance response times. By combining affordability, scalability, and real-time monitoring, the proposed system represents a meaningful step forward in innovative grid fault detection technologies, directly addressing the shortcomings of existing methods.

3. Methodology

The methodology adopted in this study is based on the design and development of a laboratory-scale IoT-enabled prototype for fault detection, classification, and localization in a three-phase power transmission system. The methods and results are derived from the second author's bachelor's thesis [20], which included both simulation and prototype studies. In the present work, only the prototype design and results are discussed, as including both would exceed the scope of this paper.

The proposed system integrates hardware and software modules to ensure accurate monitoring and fault management. At the data acquisition layer, an Arduino Mega is employed to collect real-time current values from ACS712 current sensors installed at the sending end of the transmission line model. The Arduino Mega was chosen for its multiple input channels, allowing simultaneous sensor sampling. For computational tasks, including fault classification, decision-making, and cloud communication, an ESP32 microcontroller is used owing to its higher processing capability, faster response time, and integrated Wi-Fi module. This division of tasks ensures reliable current capture by the Arduino Mega and efficient data processing by the ESP32.

The experimental setup divides the transmission line into four distinct zones by connecting resistors in parallel, thereby simulating line segments of 2 km, 4 km, 6 km, and 8 km, respectively. Each zone is continuously monitored using ACS712 sensors, and any deviation in current flow is used as an indicator for po-

tential fault conditions. Six fault scenarios are considered in this study: single line-to-ground (SLG) faults, namely red-to-ground (RG), yellow-to-ground (YG), and blue-to-ground (BG), and double line-to-ground (DLG) faults, namely red-yellow-to-ground (RYG), yellow-blue-to-ground (YBG), and red-blue-to-ground (RBG). For each of these fault types, tests are conducted across all four zones, yielding a total of 24 experimental cases.

In other words, the prototype consists of three main modules: current sensing and fault detection, data processing and classification, and communication and fault localization. For current sensing and fault detection, the Arduino Mega continuously samples currents from the ACS712 sensors at a raw sampling rate of about 9.6 kHz. Within each 500 ms acquisition window, the getVPP_*() function acts as a windowed peak detector by recording the maximum and minimum ADC values, converting their difference into the corresponding peak-to-peak voltage. This measured voltage is then used to calculate the RMS current. At the same time, the processed RMS values are updated every 1 second per channel due to the 20-sample averaging loop with 50 ms delay, resulting in an overall update of all four sensor channels approximately once every 4 seconds, sufficient to capture fault transients while balancing computational demand. A threshold-based algorithm is implemented on the ESP32 for data processing and classification. Each phase current is compared against predefined limits to distinguish between regular operation, SLG, and DLG faults. Once thresholds are exceeded, the algorithm identifies the fault types by evaluating the combination of affected phases. Lastly, for communication and fault localization, A NEO-6MV2 GPS module provides positional data, which is transmitted alongside fault information by the ESP32 through its Wi-Fi interface to the Arduino IoT Cloud. This enables remote visualization and monitoring of fault events. The reported localization error is within ±5 meters, sufficient for practical field applications.

Validation of the system was carried out through repeated hardware experiments. Each of the 24 cases was executed 40 times to ensure statistical detection, classification, and localization robustness. A detection matrix summarizing all tested fault types and line-zone combinations is provided in Table 1.

Table 1. Detection matrix of simulated fault types and line-zones combinations.

Zone (km)	SLG: RG	SLG: YG	SLG: BG	DLG: RYG	DLG: YBG	DLG: RBG
2	To be tested	To be tested	To be tested	To be tested	To be tested	To be tested
4	To be tested	To be tested	To be tested	To be tested	To be tested	To be tested
6	To be tested	To be tested	To be tested	To be tested	To be tested	To be tested
8	To be tested	To be tested	To be tested	To be tested	To be tested	To be tested

Although the prototype is based on a reduced single-phase model for hardware simplicity, fault scenarios such as SLG and DLG were successfully emulated, and their behaviours were extrapolated to reflect three-phase system conditions. This substitution introduces some limitations in replicating exact three-phase transients, which are acknowledged as a constraint of the prototype stage.

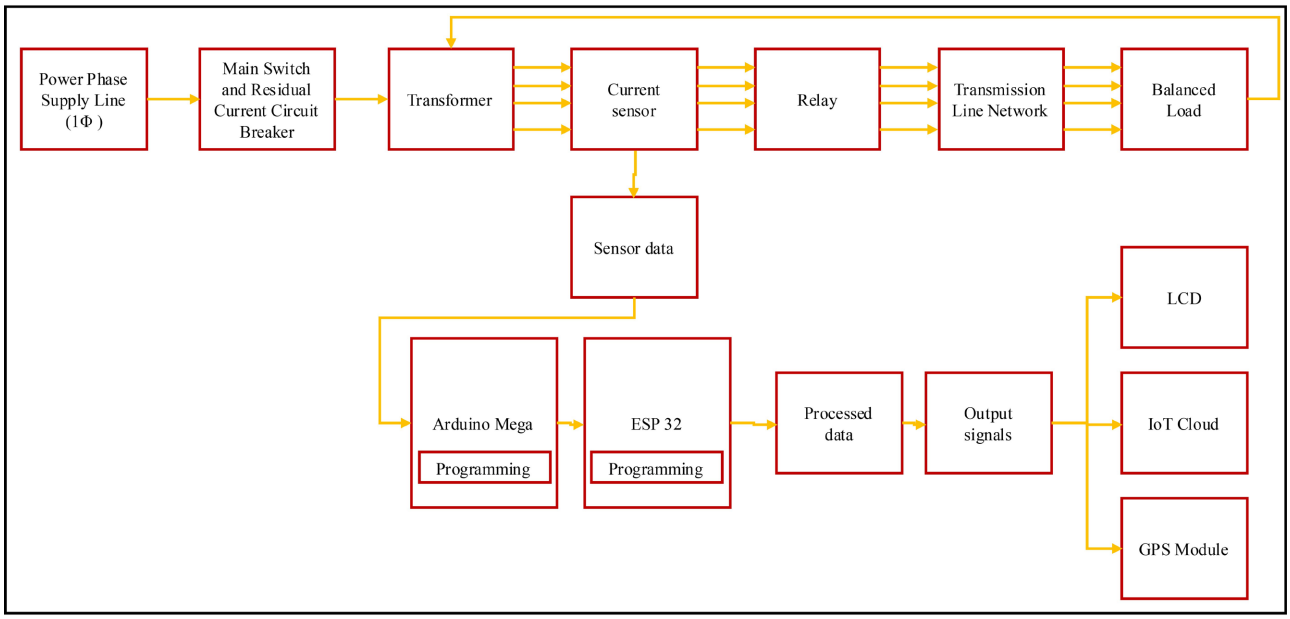

Figure 3. Block diagram of the proposed Wi-Fi and GPS-based smart monitoring and fault detection system.

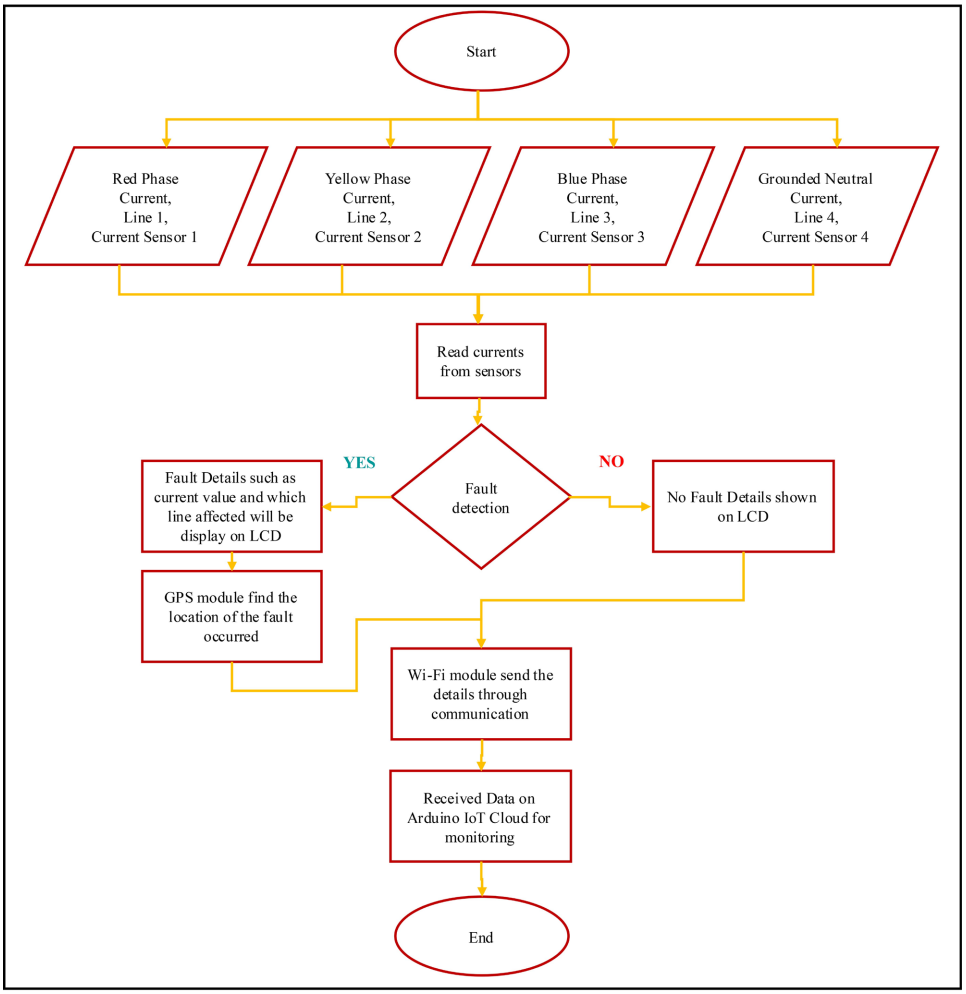

Figure 4. Summarized process flowchart of the overall system, from data acquisition to decision-making.

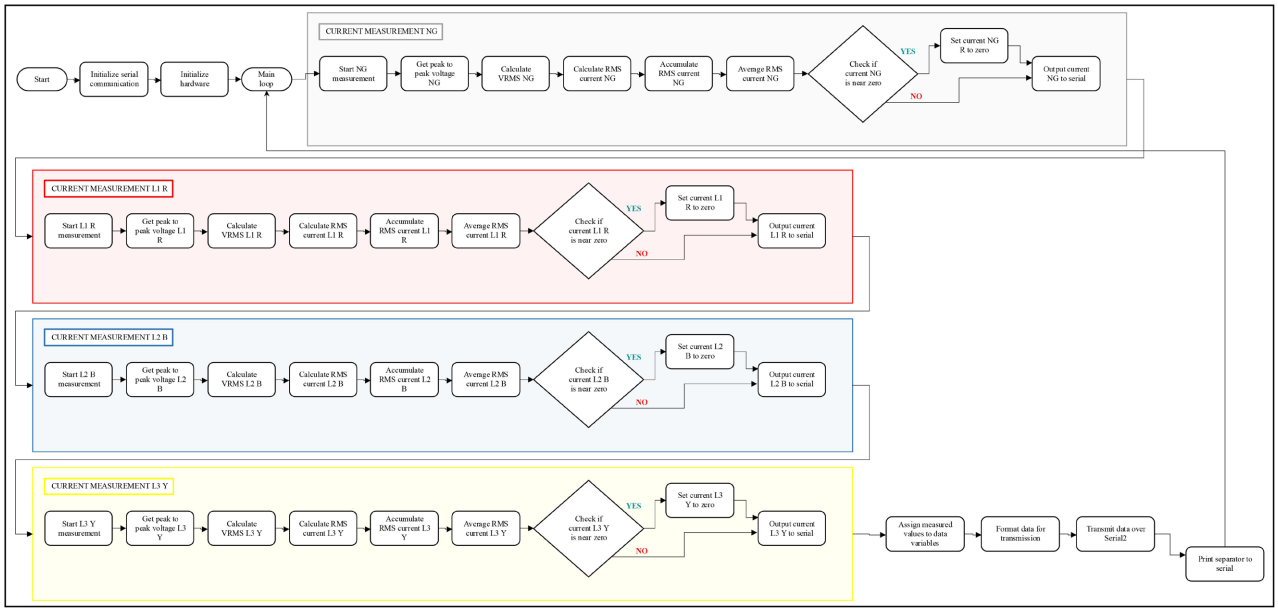

Figure 5. Arduino Mega coding flowchart for data acquisition using the ACS712 current sensor.

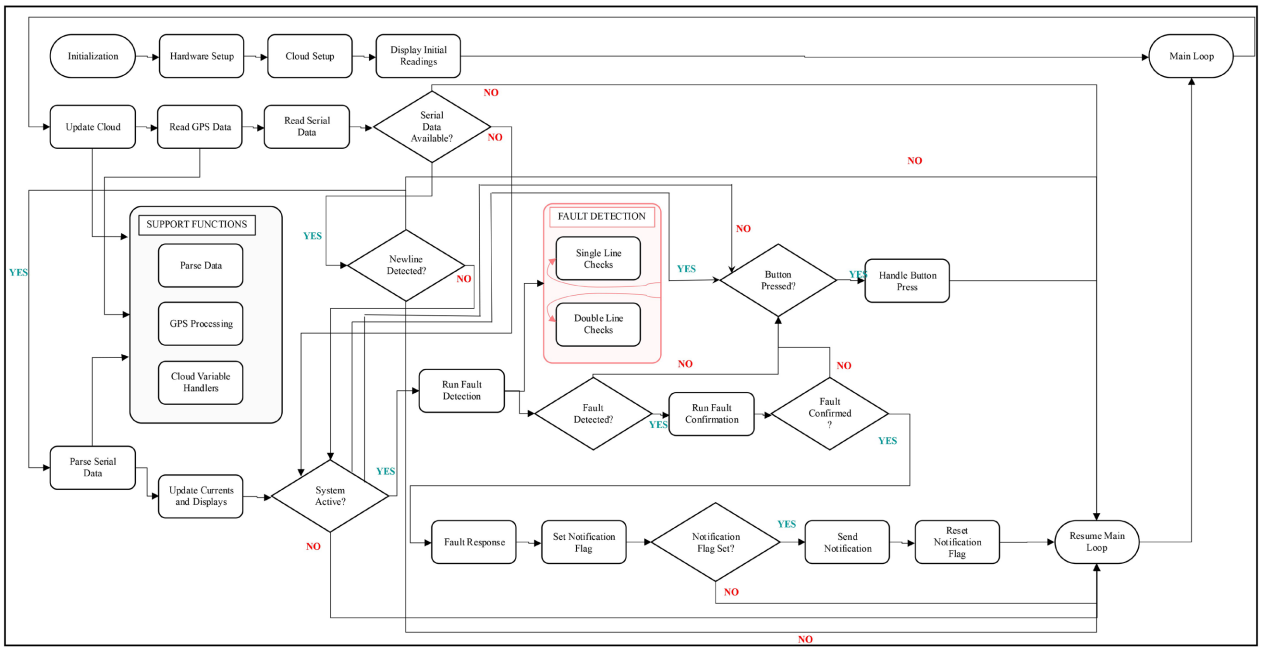

Figure 6. ESP32 coding flowchart for fault detection, classification, and localization using Arduino IoT Cloud and GPS module.

Regarding communication, the ESP32 demonstrated average transmission delays of less than 5000 ms, acceptable for small-scale IoT deployments. Nevertheless, scalability and cybersecurity challenges, such as authentication, data integrity, and network congestion, must be considered before field-scale deployment.

Four diagrams are included to illustrate the methodology further. Figure 3 presents the block diagram of the proposed system, showing the integration of current sensors, controllers, and IoT components. Figure 4 depicts the summarized flowchart of the overall process, from sensing to decision-making. Figure 5 details

the Arduino Mega coding flowchart for data acquisition using ACS712 sensors. Figure 6 presents the ESP32 coding flowchart, showing the processing of fault detection, classification, and localization, along with its integration with the Arduino IoT Cloud and GPS module. Figure 5 and Figure 6 are adapted from [20] and originate from the thesis's prototype implementation. For readers seeking more profound insights into the coding logic and simulation aspects, reference can be made to the thesis.

4. Results and Discussion

This section presents the experimental results and analysis of the developed hardware prototype, which emulates a simplified single-phase parallel configuration to replicate the behaviour of a three-phase transmission line. The discussion begins with the evaluation of the system's current-voltage characteristics, impedance profiles, and load response under balanced (no-fault) operating conditions, establishing a baseline reference. It then proceeds to faulted conditions, where single-line-to-ground (SLG) and double-line-to-ground (DLG) events are captured and analysed to validate the accuracy of fault detection and classification. Finally, the overall performance of the complete Wi-Fi and GPS-enabled DCL system is demonstrated, highlighting its capability to detect, classify, and localize faults with high precision.

4.1. Balanced Transmission Line Load Flow (No fault Condition)

The prototype transmission line was initially tested under a balanced load condition to establish a baseline reference for subsequent fault analysis. The circuit was energised with a 12 V_{RMS} supply at 50 Hz, and divided into four distinct zones, each represented by a 10 Ω resistor to emulate the cumulative impedance of transmission segments (equivalent to 2 km per zone). A single-phase four-wire configuration was employed, consisting of three parallel conductors representing red, yellow, and blue phases, along with a neutral return line. At the receiving end, three LED-based loads were connected, each phase comprising three LEDs (forward voltage 2.2 V, current rating 20 mA) in series with a 700 Ω resistor, thereby ensuring symmetrical loading. Figure 7(a) and Figure 7(b) illustrate the transmission line tower management with its four impedance zones and the balanced LED load bank.

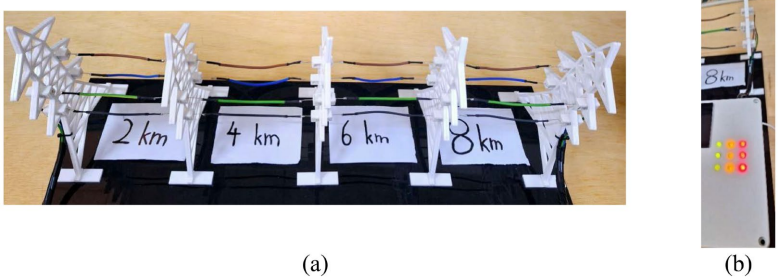

(a) (b)

Figure 7. (a) 12 V transmission line tower with power lines divided into 4 zones. (b) Balanced LED load connected at the receiving end.

Tables 2-5 summarise the measured resistance, voltage, and current values for the Red, Yellow, Blue, and Neutral conductors. As observed in Table 2, the red phase shows uniform current (I_{RMS} = 0.016 A) across all resistors and the load. Each of the four resistors, R1 to R4, experiences a voltage drop of 0.16 V_{RMS}, while the terminal load receives 11.84 V_{RMS}. The total cumulative impedance along the red line increases incrementally (10 Ω, 20 Ω, 30 Ω, and 40 Ω), and the corresponding voltage drop accumulates accordingly (0.16 V_{RMS}, 0.32 V_{RMS}, 0.48 V_{RMS}, and 0.64 V_{RMS}), culminating in a total voltage drop of 11.84 V_{RMS} from source to load. An identical pattern is evident for the yellow and blue phases, as presented in Tables 3-4. All live phases exhibit identical current flow of 0.016 A across each resistor and the terminal load, with matching voltage drops of 0.16 V_{RMS} per resistor and 11.84 V_{RMS} across the load. This consistency across all three phases confirms a perfectly balanced system under the no-fault condition.

Table 2. Resistance, voltage, and current parameters for red phase line.

Resistor	R1	R2	R3	R4	Load
Resistance, Ω	10	10	10	10	700
Voltage across the resistor, V_{RMS}	0.16	0.16	0.16	0.16	11.2
Current, I_{RMS}	0.016	0.016	0.016	0.016	0.016
Summation of line impedance along red phase wire, Ω_T	10	20	30	40	NA
Summation of voltage drop resistor, V_{TRMS}	0.16	0.32	0.48	0.64	11.84

Table 3. Resistance, voltage, and current parameters for yellow phase line.

Resistor	R1	R2	R3	R4	Load
Resistance, Ω	10	10	10	10	700
Voltage across the resistor, V_{RMS}	0.16	0.16	0.16	0.16	11.2
Current, I_{RMS}	0.016	0.016	0.016	0.016	0.016
Summation of line impedance along red phase wire, Ω_T	10	20	30	40	NA
Summation of voltage drop resistor, V_{TRMS}	0.16	0.32	0.48	0.64	11.84

Table 4. Resistance, voltage, and current parameters for blue phase line.

Resistor	R1	R2	R3	R4	Load
Resistance, Ω	10	10	10	10	700
Voltage across the resistor, V_{RMS}	0.16	0.16	0.16	0.16	11.2
Current, I_{RMS}	0.016	0.016	0.016	0.016	0.016
Summation of line impedance along red phase wire, Ω_T	10	20	30	40	NA
Summation of voltage drop resistor, V_{TRMS}	0.16	0.32	0.48	0.64	11.84

Table 5. Resistance, voltage, and current parameters for neutral line.

Resistor	R1	R2	R3	R4	Load
Resistance, Ω	10	10	10	10	130.61
Voltage across the resistor, V_{RMS}	0.660	0.660	0.660	0.660	8.62
Current, I_{RMS}	0.066	0.066	0.066	0.066	0.066
Summation of line impedance along red phase wire, Ω_T	10	20	30	40	NA
Summation of voltage drop resistor, V_{TRMS}	0.660	1.32	1.98	2.64	11.26

In contrast, the Neutral line displays distinct electrical characteristics due to the parallel emulation of the three-phase star system. As shown in Table 5, the measured neutral current was significantly higher at 0.066 A than the phase currents. This is not indicative of system imbalance but rather a direct consequence of the chosen emulation method, wherein all return currents from the three parallel phases are combined in the neutral conductor. In an ideal three-phase star-connected system with balanced loads, the instantaneous sum of the three-phase current equals zero, resulting in negligible neutral current. However, in this single-phase emulation, the measured neutral current corresponds to the cumulative effect of the three live phase returns. The voltage drops across the neutral line resistors are consequently larger, measured at 0.660 V_{RMS} per resistor, increasing cumulatively to 2.64 V_{RMS} by R4, before delivering 8.62 V_{RMS} to the terminal load with a resistance of 130.61 Ω. The total voltage drop in the Neutral line again sums to 11.26 V_{RMS}, which is in agreement with the supply.

These findings confirm that the constructed hardware prototype successfully replicates the key characteristics of a three-phase star-to-star transmission line within a scaled single-phase configuration. The uniform current and voltage distribution across all three emulated phases, the predictable linear impedance-voltage relationship, and the expected accumulation of return currents in the neutral conductor collectively validate the fidelity of the model. Establishing this balanced reference condition is critical, as it provides the benchmark against which deviations arising from single line to ground (SLG) and double line to ground (DLG) fault scenarios can be clearly identified and analysed in subsequent sections.

4.2. Result and Analysis of SLG and DLG Faults

The fault analysis was performed on the same balanced transmission line hardware to investigate the impact of single-line-to-ground (SLG) and double-line-to-ground (DLG) faults. Each fault was introduced sequentially at four predefined area zones of the transmission lines, corresponding to cumulative impedance values of 10 Ω (2 km), 20 Ω (4 km), 30 Ω (6 km), and 40 Ω (8 km). The results presented here focus first on SLG faults, with DLG faults analysed in the subsequent section.

4.2.1. Single Line to Ground (SLG) Fault

The single line to ground (SLG) fault was simulated on the red phase conductor at four fault locations corresponding to 2 km, 4 km, 6 km, and 8 km along the transmission line, representing cumulative impedances of 10 Ω, 20 Ω, 30 Ω, and 40 Ω, respectively. The SLG fault was induced by shorting the red phase to ground using a jumper connection. Figure 8 shows the physical fault establishment at different zones of the transmission line. The results showing the corresponding graphical representation of the SLG fault at each location are shown in Figures 9-16.

At the 2 km fault location, the measured voltage drop across the first resistor of the Red Phase line was 2.52 V, while the current in the Red Phase was 0.252 A. This behaviour is illustrated in Figure 9, which shows the distribution of voltage drop and current with respect to line impedance. The neutral line also reflected a nearly identical response, with a voltage drop of 2.63 V and a corresponding current of 0.263 A, as depicted in Figure 10. This synchronous behaviour between the faulted phase and the neutral path confirms the expected current return mechanism in SLG faults.

Figure 8. Single line to ground (SLG) fault on the red phase at (a) 2 km, (b) 4 km, (c) 6 km, and (d) 8 km.

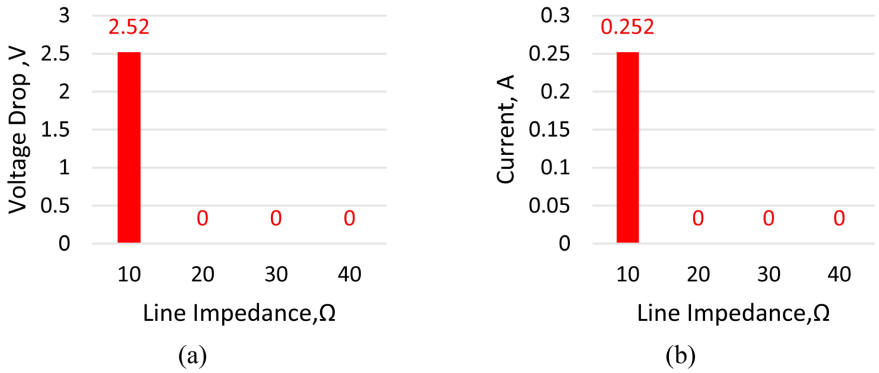

Figure 9. SLG fault at 2 km zone, (a) Voltage drop across each resistor of red phase line (V_{RRMS}) vs line impedance along the transmission line, (Ω_{RT}), and (b) Current along the red phase line (I_{RRMS}) vs line impedance along the transmission line, (Ω_{RT}).

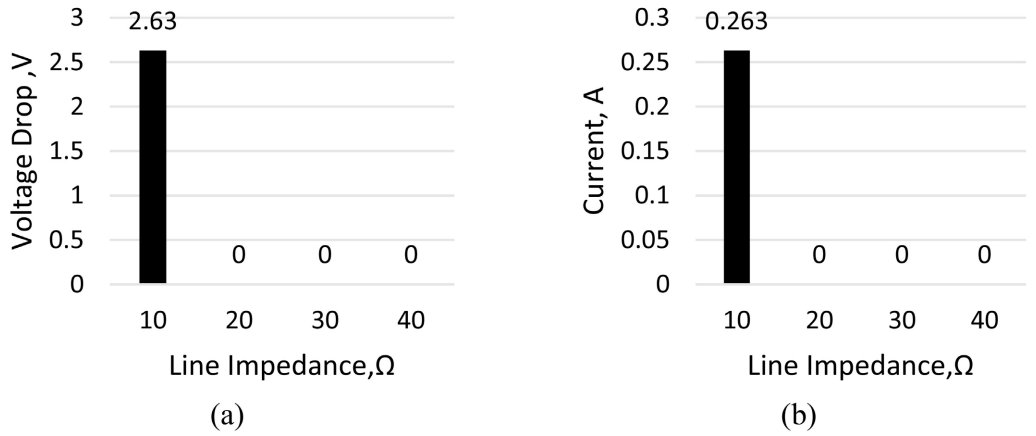

Figure 10. SLG fault occurred at zone 2 km (a) Voltage drop across each resistor of neutral line (V_{Nrms}) vs line impedance along the transmission line, (Ω_{NT}) and (b) Current along the neutral line, (I_{NRMS}) vs line impedance along the transmission line, (Ω_{NT}).

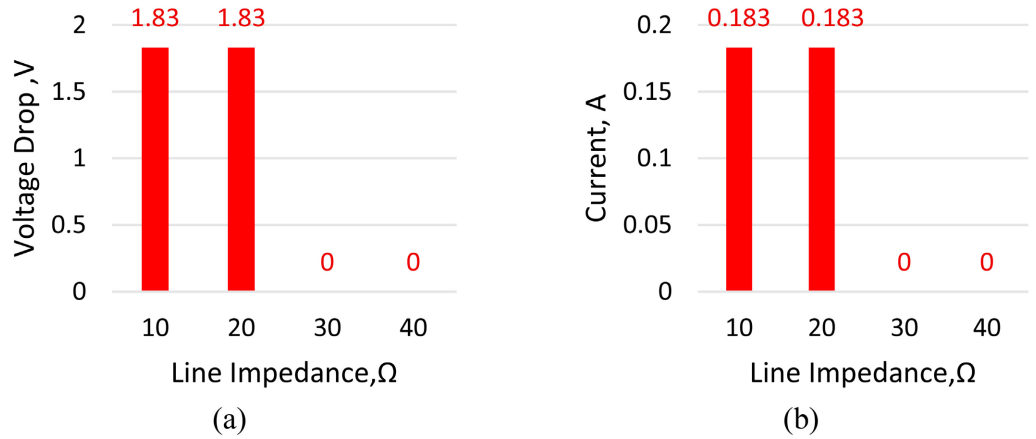

Figure 11. SLG fault occurred at zone 4 km, (a) Voltage drop across each resistor of red phase line (V_{RRMS}) vs line impedance along the transmission line, (Ω_{RT}) and (b) Current along the red phase line (I_{RRMS}) vs line impedance along the transmission line, (Ω_{RT}).

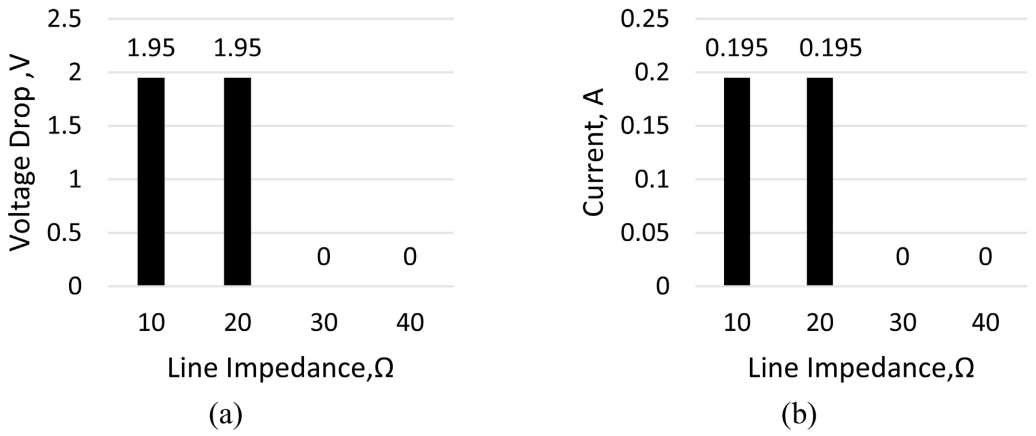

Figure 12. SLG fault occurred at zone 4 km, (a) Voltage drop across each resistor of neutral line (V_{Nrms}) vs line impedance along the transmission line, (Ω_{NT}) and (b) Current along the neutral line, (I_{NRMS}) vs line impedance along the transmission line, (Ω_{NT}).

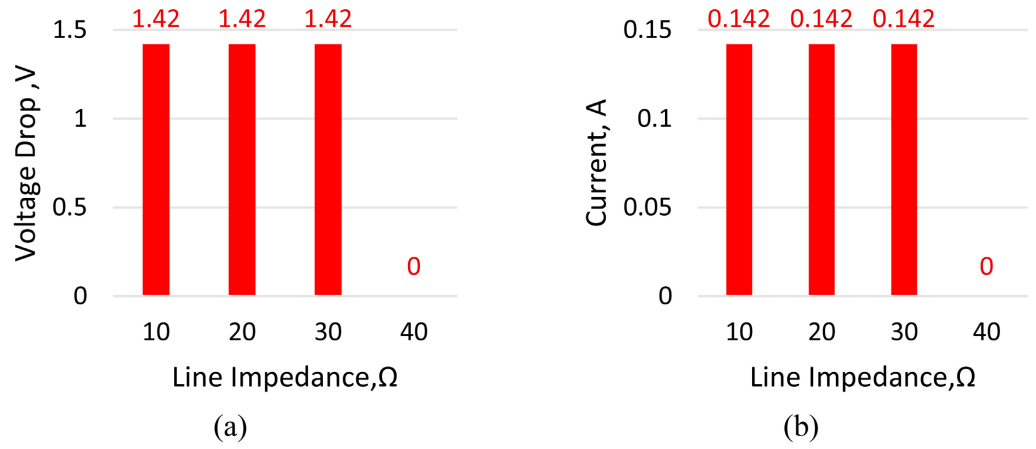

Figure 13. SLG fault occurred at zone 6 km, (a) Voltage drop across each resistor of red phase line (V_{RRMS}) vs line impedance along the transmission line, (Ω_{RT}), and (b) Current along the red phase line (I_{RRMS}) vs line impedance along the transmission line, (Ω_{RT}).

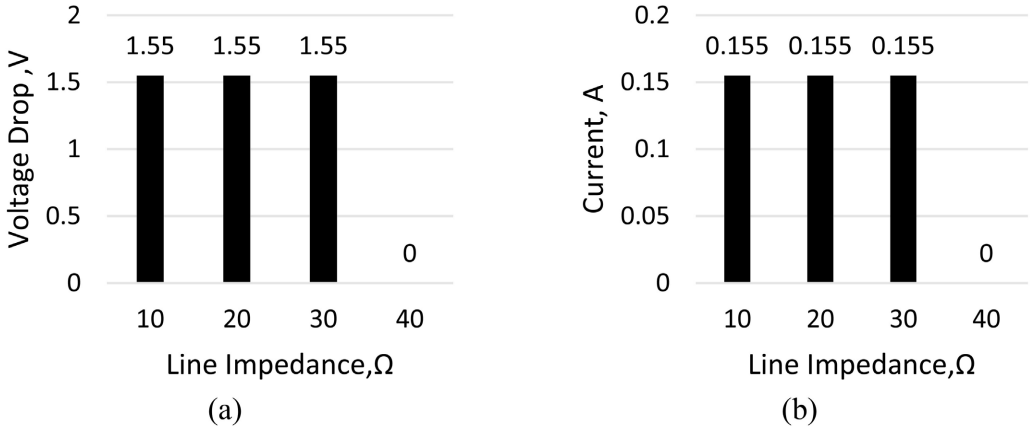

Figure 14. SLG fault occurred at zone 6 km, (a) Voltage drop across each resistor of neutral line (V_{Nrms}) vs line impedance along the transmission line, (Ω_{NT}) and (b) Current along the neutral line, (I_{NRMS}) vs line impedance along the transmission line, (Ω_{NT}).

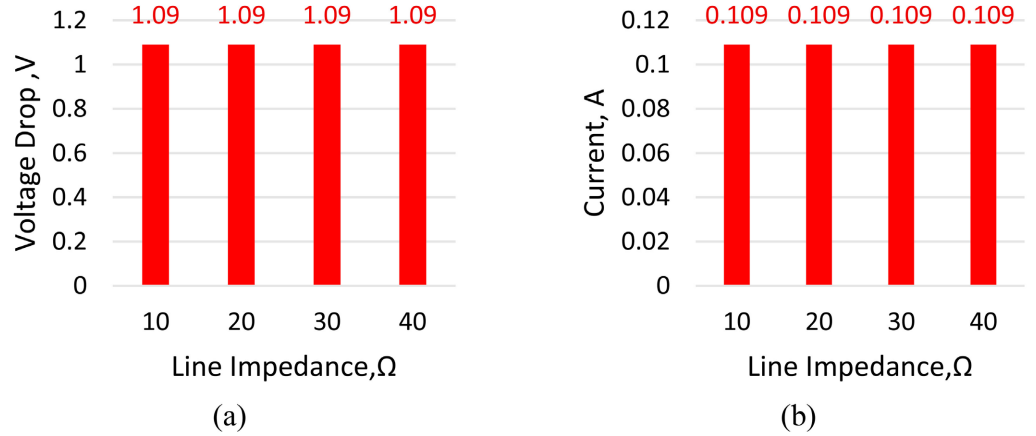

Figure 15. SLG fault occurred at zone 8 km, (a) Voltage drop across each resistor of red phase line (V_{RRMS}) vs line impedance along the transmission line, (Ω_{RT}), and (b) Current along the red phase line (I_{RRMS}) vs line impedance along the transmission line, (Ω_{RT}).

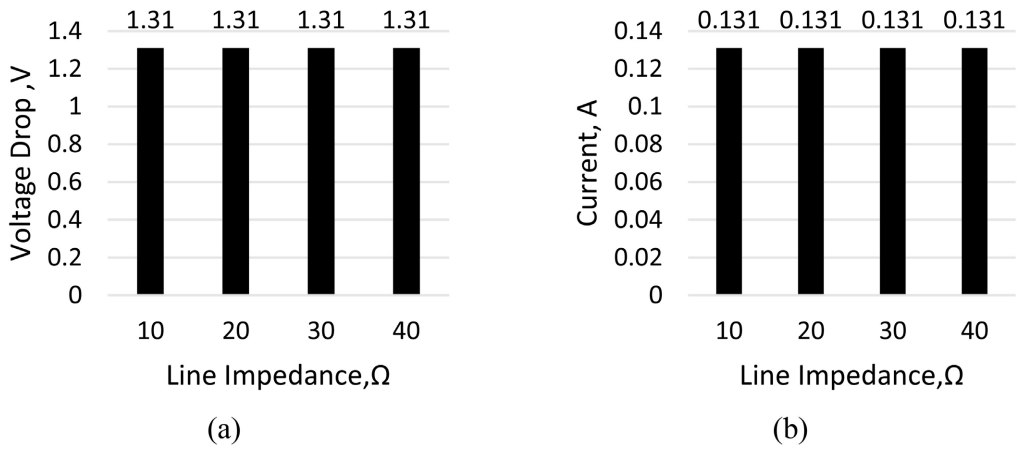

Figure 16. SLG Fault occurred at zone 8 km, (a) Voltage drop across each resistor of neutral line (V_{Nrms}) vs line impedance along the transmission line, (Ω_{NT}) and (b) Current along the neutral line, (I_{NRMS}) vs line impedance along the transmission line, (Ω_{NT}).

When the fault was shifted to 4 km, the Red Phase exhibited a reduced voltage drop of 1.83 V per resistor, yielding a cumulative 3.66 V along the faulted section. The corresponding current decreased to 0.183 A, consistent with the higher fault impedance. The neutral line also displayed a proportional voltage drop of 1.95 V, with current along the neutral reaching 0.195 A. These results are clearly visualised in **Figure 11** and **Figure 12**, which demonstrate that the propagation of fault effects becomes distributed as the distance from the source increases.

At the 6 km fault point, the Red Phase resistors exhibited a consistent voltage drop of 1.42 V each up to the third resistor, producing a cumulative voltage of 4.26 V across the line. The current along the Red Phase measured 0.142 A, and the neutral line displayed almost identical magnitudes with 1.55 V per resistor and a corresponding current of 0.155 A. This behaviour is represented graphically in **Figure 13** and **Figure 14**, where the systematic reduction in fault current and voltage drop magnitude with increasing distance is clearly evident.

Finally, the 8 km fault showed the lowest Red Phase current of 0.109 A, with each of the four resistors experiencing a voltage drop of 1.09 V. The cumulative voltage across the line was 4.36 V, while the neutral line mirrored this pattern with a drop of 1.31 V per resistor and 0.131 A current. These trends are illustrated in **Figure 15** and **Figure 16**, which confirm the proportional relationship between fault distance, voltage distribution, and current magnitude.

The overall analysis of **Figures 9-16** reveals a systematic inverse relationship between the fault distance and fault current, with current magnitude decreasing as the fault location is moved further along the line. Simultaneously, the cumulative voltage distribution across both the Red Phase and Neutral lines follows a consistent, predictable pattern. This observation demonstrates the linear scalability of SLG fault characteristics along the transmission line, validating the potential for distance-based fault localisation. Furthermore, as the response pattern was consistent for the Red Phase, it was deemed unnecessary to repeat the SLG tests for Yellow-to-Ground and Blue-to-Ground cases, since the same proportional re-

lationships are expected across all three phases.

4.2.2. Double Line to Ground (DLG) Fault

In this section, the behaviour of the transmission line model under Double Line to Ground (DLG) faults was examined, specifically considering faults between the red and yellow phases to ground at different fault locations (2 km, 4 km, 6 km, and 8 km). The DLG fault was induced by shorting the red phase and yellow phase to ground using two jumper connections. Figure 17 shows the physical fault establishment at different zones of the transmission line. The recorded results together with their corresponding graphical representations are presented in Figures 18-25.

As illustrated in Figure 18 and Figure 19, the occurrence of a DLG fault close to the sending end (2 km) caused a pronounced voltage drop across the first resistors of both the red and yellow phase lines, measured at approximately 1.4 V and 1.5 V, respectively. Correspondingly, the line currents increased sharply to 0.14 A in the Red phase and 0.15 A in the Yellow phase. The neutral line response was equally significant, registering a 3 V drop across the first resistor with a neutral current of 0.30 A. This indicates strong ground coupling when the fault occurs near the source. Beyond this first zone, the voltage and current values diminished rapidly to zero, providing clear evidence of fault localisation close to the sending end.

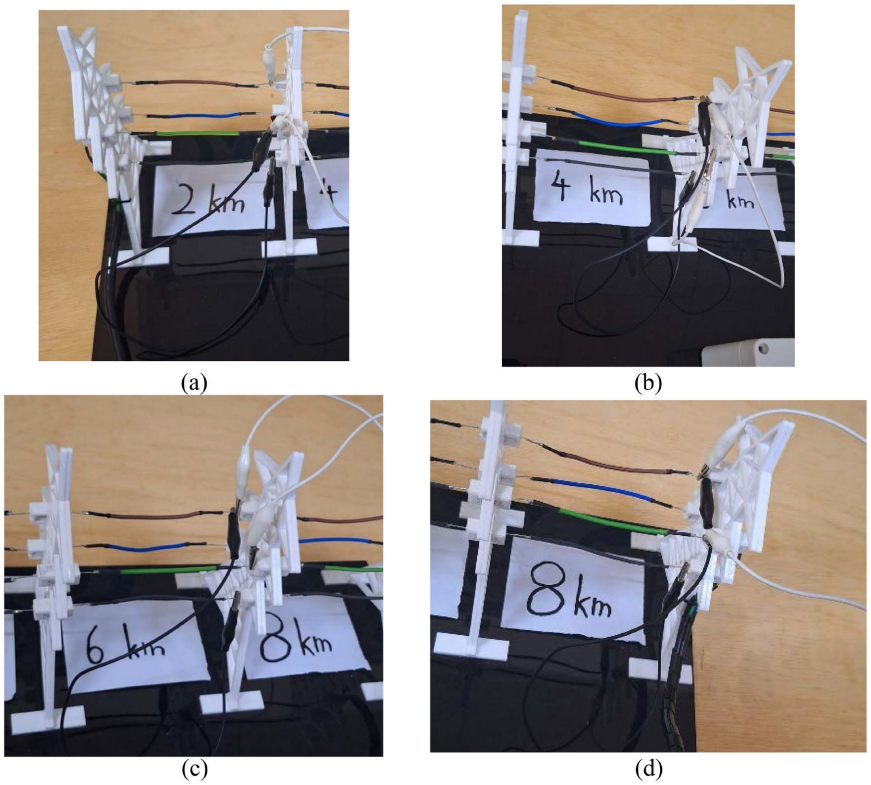

Figure 17. Double Line to Ground Fault Established, Red and Yellow Phase to Ground Fault, at (a) 2 km, (b) 4 km, (c) 6 km, and (d) 8 km.

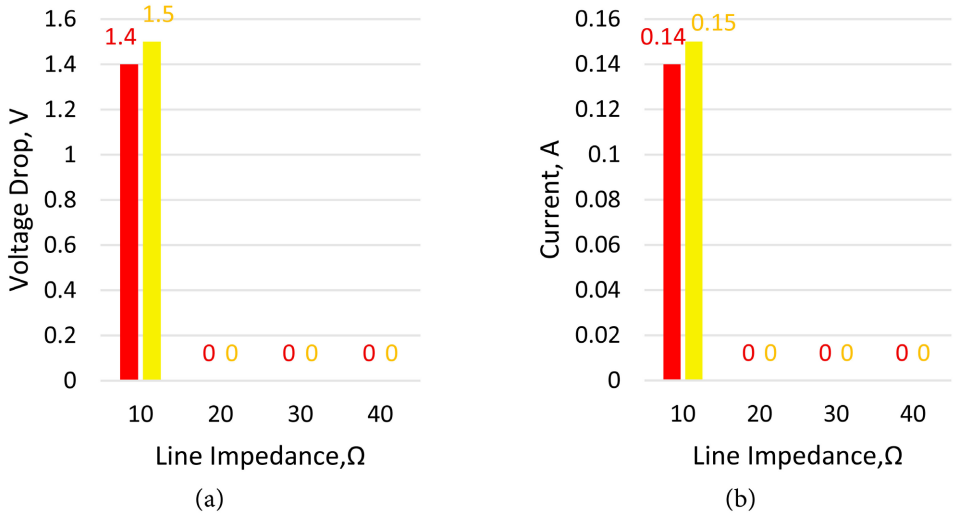

Figure 18. DLG fault occurred at zone 2 km, (a) Voltage drop across each resistor of red phase line (V_{RRMS}), voltage drop across each resistor of yellow phase line (V_{YRMS}) vs line impedance along the transmission line, (Ω_T), and (b) Current along the red phase line (I_{RRMS}), current along the yellow phase line (I_{YRMS}) vs line impedance along the transmission line, (Ω_T).

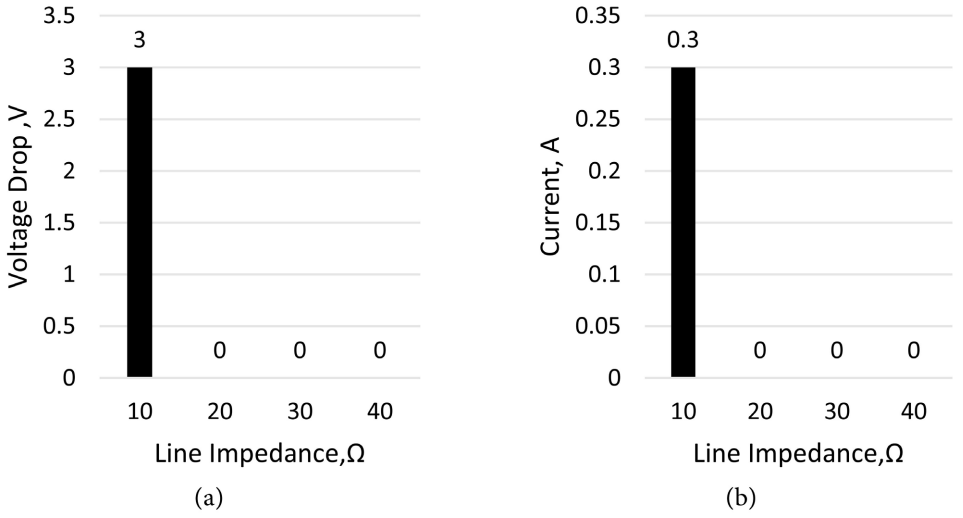

Figure 19. DLG Fault occurred at zone 2 km, (a) Voltage drop across each resistor of neutral line (V_{Nrms}) vs line impedance along the transmission line, (Ω_{NT}) and (b) Current along the neutral line, (I_{NRMS}) vs line impedance along the transmission line, (Ω_{NT}).

When the fault was applied at 4 km, as shown in **Figure 20** and **Figure 21**, the voltage drops became distributed across the first two resistors of both red and yellow phases, with values in the range of 1.07 - 1.10 V. The associated phase currents were approximately 0.107 - 0.110 A. For the neutral line, the cumulative voltage drop reached 2.25 V at the first resistor and increased linearly up to 4.51 V across the line, producing a neutral current of about 0.225 A. Compared with the 2 km case, the fault influence extended further along the line. However, the overall magnitude of the voltage and current response decreased slightly, highlighting the attenuation effect with distance.

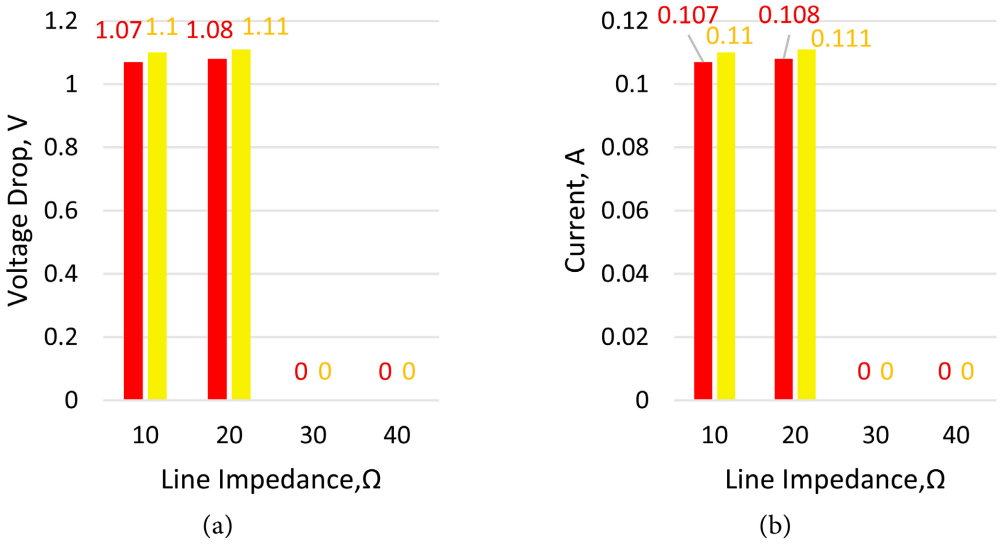

Figure 20. DLG fault occurred at zone 4 km, (a) Voltage drop across each resistor of red phase line (V_{RRMS}), voltage drop across each resistor of yellow phase line (V_{YRMS}) vs line impedance along the transmission line, (Ω_T), and (b) current along the red phase line (I_{RRMS}), current along the yellow phase line (I_{YRMS}) vs line impedance along the transmission line, (Ω_T).

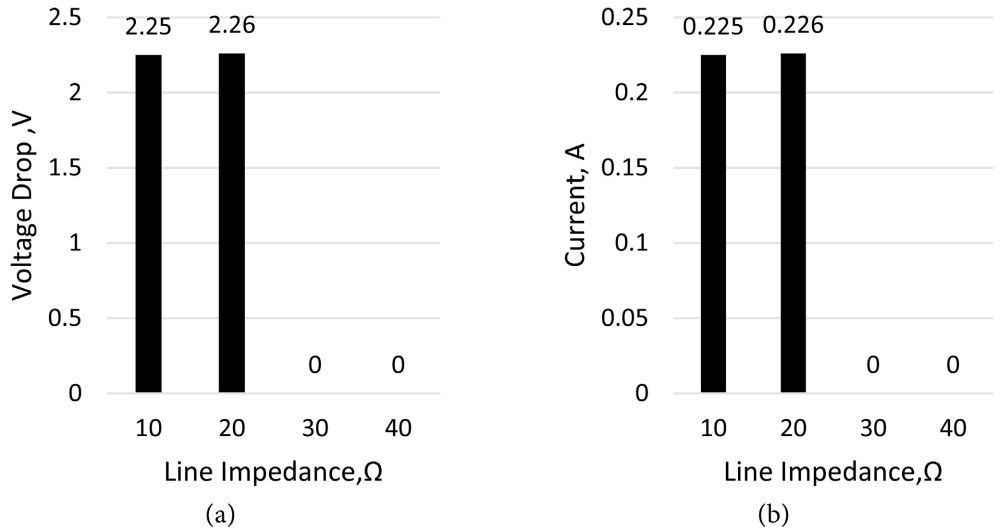

Figure 21. DLG fault occurred at zone 4 km, (a) Voltage drop across each resistor of neutral line (V_{Nrms}) vs line impedance along the transmission line, (Ω_{NT}) and (b) Current along the neutral line, (I_{NRMS}) vs line impedance along the transmission line, (Ω_{NT}).

At 6 km, as illustrated in **Figure 22** and **Figure 23**, the effects of the fault extended even further. Both Red and Yellow phases experienced uniform voltage drops of approximately 0.87 - 0.88 V across three resistors, with corresponding phase currents of 0.087 - 0.088 A. The neutral line response followed a distributed pattern, showing a voltage drop of about 1.82 V across each resistor up to the third, accompanied by a neutral current of 0.182 A. Compared to the 4 km case, the fault magnitude decreased further, reinforcing the trend that as fault distance increases, the phase and neutral fault currents diminish progressively.

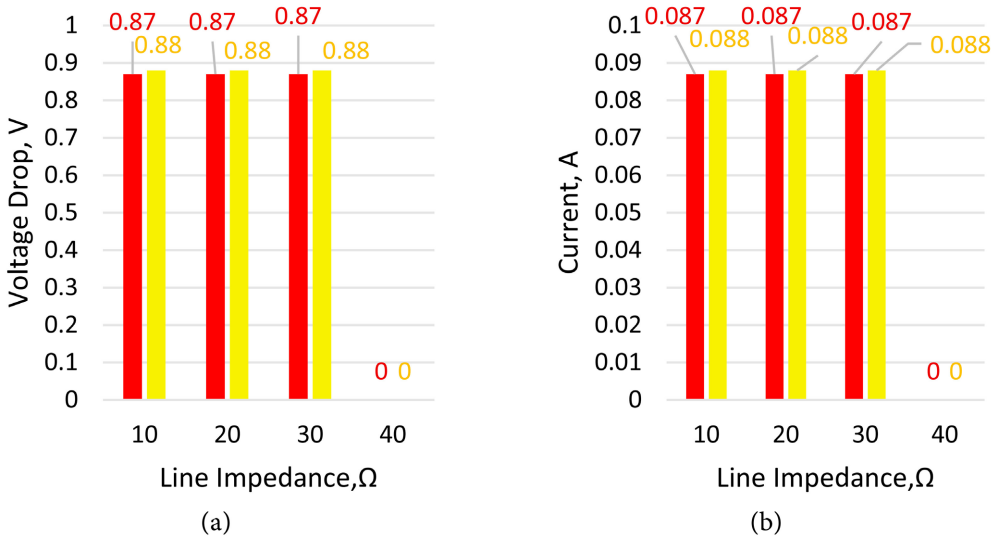

Figure 22. DLG fault occurred at zone 6 km, (a) Voltage drop across each resistor of red phase line (V_{RRMS}), voltage drop across each resistor of yellow phase line (V_{YRMS}) vs line impedance along the transmission line, (Ω_T), and (b) Current along the red phase line (I_{RRMS}), current along the yellow phase line (I_{YRMS}) vs line impedance along the transmission line, (Ω_T).

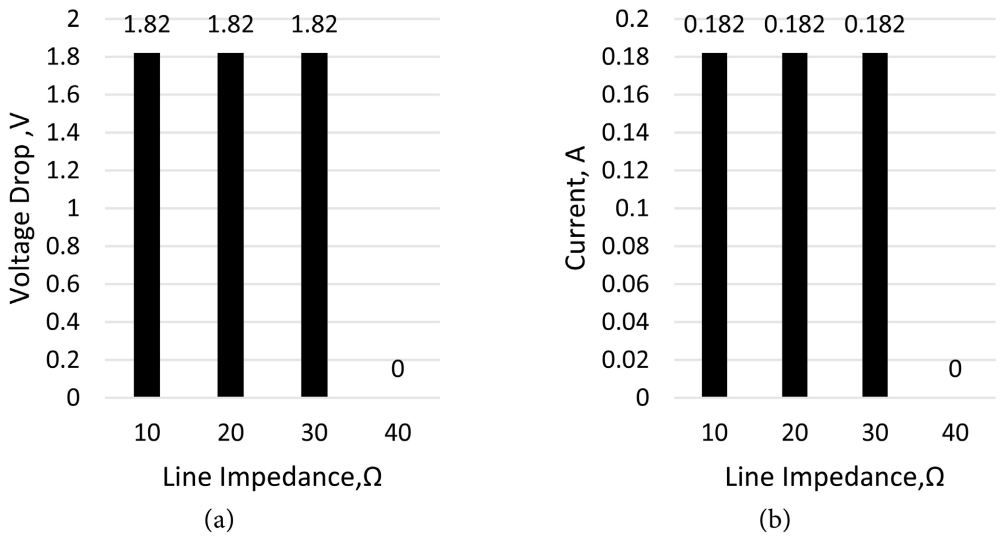

Figure 23. DLG fault occurred at zone 6 km, (a) Voltage drop across each resistor of neutral line (V_{Nrms}) vs line impedance along the transmission line, (Ω_{NT}) and (b) Current along the neutral line, (I_{NRMS}) vs line impedance along the transmission line, (Ω_{NT}).

Finally, at the farthest point (8 km), the fault responses were the weakest, as shown in **Figure 24** and **Figure 25**. Both the Red and Yellow phases displayed consistent voltage drops of 0.72 V across all four resistors, with equal phase currents of 0.072 A. The neutral line exhibited a uniform drop of 1.5 V across all four resistors, with a constant neutral current of 0.150 A. The distribution here was more symmetrical compared to the other cases. Yet, the overall fault current magnitude was the lowest among all four zones, confirming the attenuation effect of line resistance over long distances.

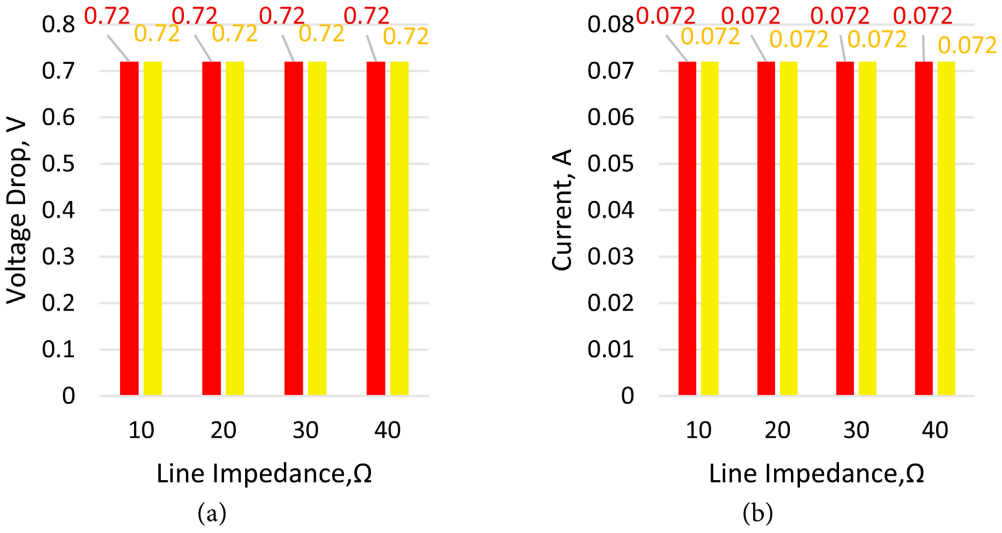

Figure 24. DLG fault occurred at zone 8 km, (a) Voltage drop across each resistor of red phase line (V_{RRMS}), voltage drop across each resistor of yellow phase line (V_{YRMS}) vs line impedance along the transmission line, (Ω_T), and (b) Current along the red phase line (I_{RRMS}), current along the yellow phase line (I_{YRMS}) vs line impedance along the transmission line, (Ω_T).

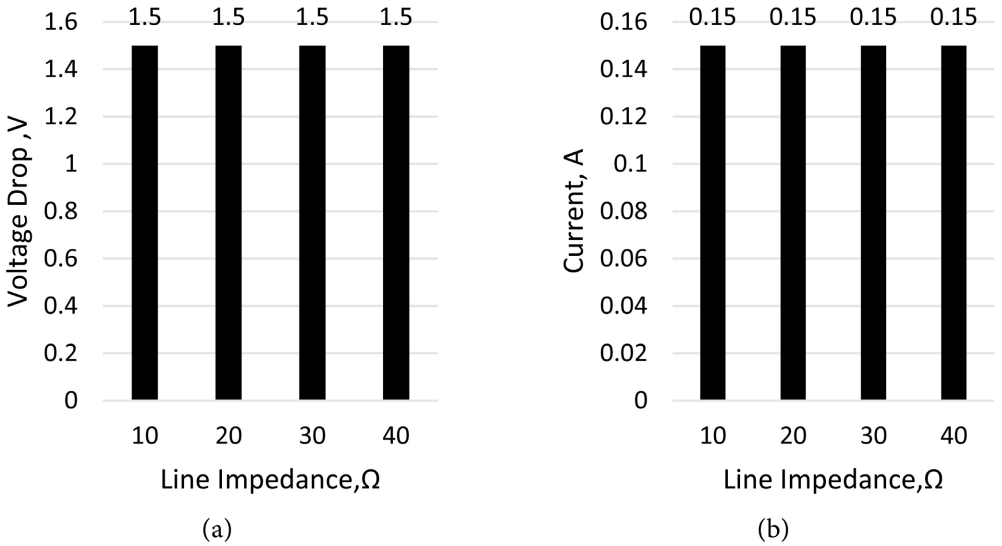

Figure 25. DLG fault occurred at zone 8 km, (a) Voltage drop across each resistor of neutral line (V_{Nrms}) vs line impedance along the transmission line, (Ω_{NT}) and (b) Current along the neutral line, (I_{NRMS}) vs line impedance along the transmission line, (Ω_{NT}).

From these four cases, several important conclusions can be drawn. First, the magnitude of voltage and current decreases with fault distance, as faults closer to the sending end produce higher fault currents (e.g., 0.30 A neutral current at 2 km vs. 0.150 A at 8 km). Second, the neutral line behaviour consistently confirms the strength of ground coupling, as it carried the highest cumulative response and is therefore effective in detecting ground-related faults. Third, the results clearly demonstrate that fault localisation is feasible, since the distribution of voltage drops across the resistors directly correlates with the fault zone; for example, at 2

km, only the first resistor shows a drop, whereas at 8 km, all resistors show uniform drops. Finally, the results indicate a systematic and predictable response, with a linear attenuation pattern observed across the four fault locations. This behaviour supports the feasibility of implementing a coding-based fault management system, as developed later through the ESP32, Arduino IoT Cloud, and GPS integration.

It should also be noted that only the Red-Yellow DLG fault was explicitly tested in this study. The Red-Blue and Yellow-Blue combinations were omitted, as the system is symmetric across all three phases, and the results would therefore be consistent and repetitive. This selective approach reduces the experimental workload while preserving analytical integrity.

4.3. Design of Wi-Fi and GPS-Based Smart Monitoring and Fault Detection System for Three-Phase Power Transmission Line Using Arduino

The fault detection, classification, and localisation (DCL) framework for the transmission line circuit was realised using the Arduino Mega and ESP32 microcontrollers. The Arduino Mega was programmed to acquire current data from the ACS712 sensors, while the ESP32 was responsible for fault classification, localisation, and IoT-based reporting. The overall coding workflow for both controllers has already been presented in **Figure 5** and **Figure 6** of the methodology section. As noted earlier, the coding logic and simulation aspects were derived from the second author's bachelor's thesis [20]. For readers seeking deeper insights into the detailed coding structure and simulation-based results, reference should be made to this thesis.

Before hardware implementation, the system design was modelled and verified in software. **Figure 26(a)** and **Figure 26(b)** show the initial circuit design and schematic diagram developed during the pre-construction phase. In contrast, **Figure 26(c)** illustrates the assembled hardware prototype of the transmission line DCL circuit.

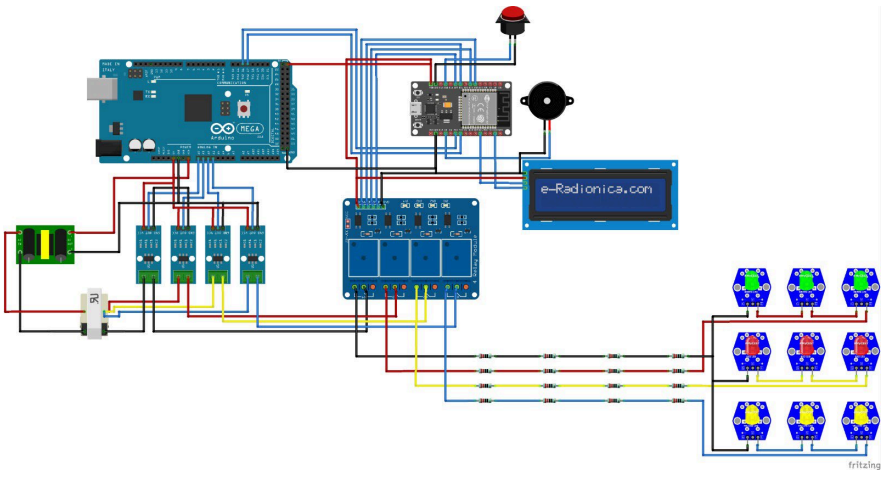

(a)

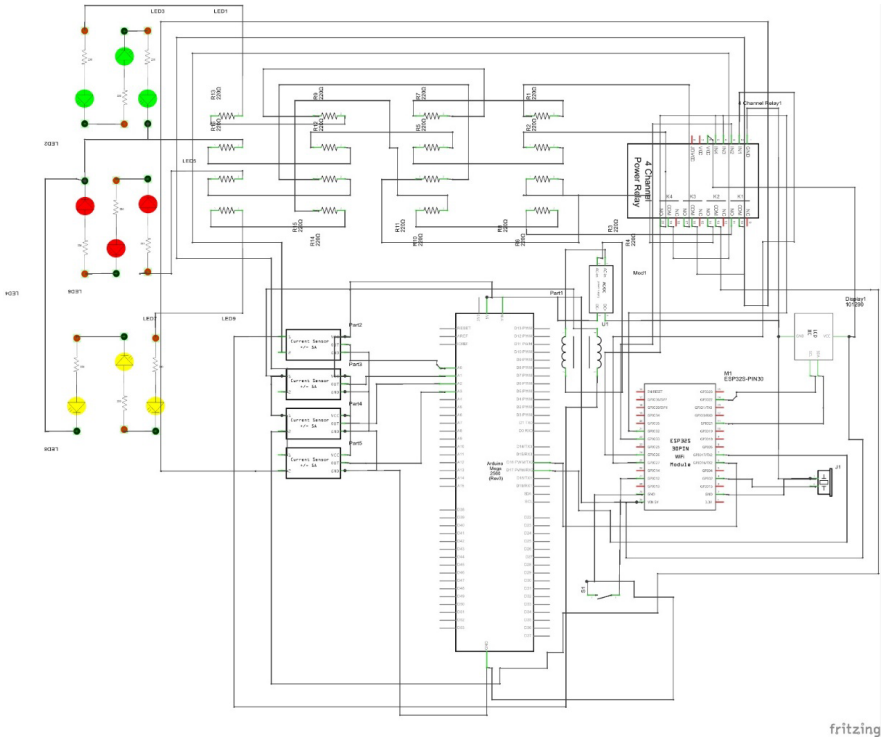

(b)

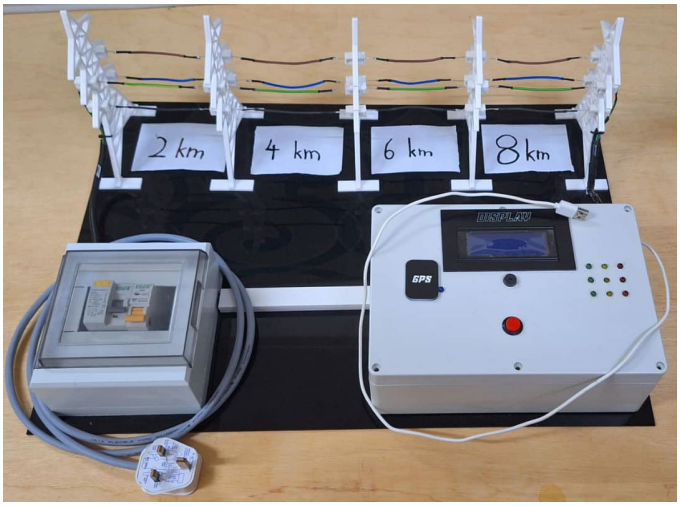

(c)

Figure 26. (a) Circuit design of the hardware system, (b) Schematic diagram of the designed circuit, and (c) the built hardware system.

During the no-fault condition, the prototype operated normally, with system status indicated on the LCD and continuous current monitoring via the Arduino IoT Cloud interface. Figure 27 demonstrates this condition, where the physical hardware is shown in Figure 27(a), the LCD confirming no fault in Figure 27(b), current monitoring and system status displayed on the IoT Cloud in Figure 27(c), and a notification confirmation in the Arduino IoT Cloud messenger in Figure 27(d).

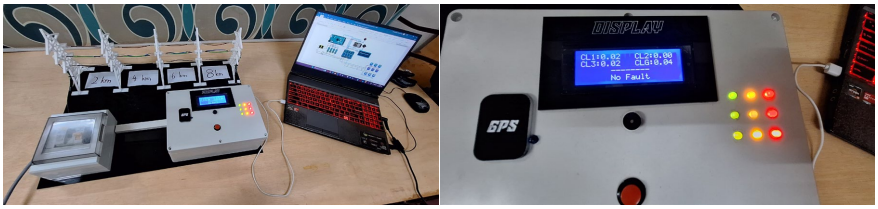

(a) (b)

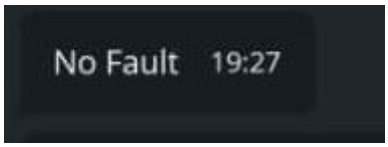

(c) (d)

Figure 27. The built prototype during no fault conditions, (a) the system, (b) LCD during no fault, (c) monitoring of line currents and status of the fault condition via Arduino IoT Cloud, and (d) fault notification displayed in the Arduino IoT Cloud Messenger.

The functionality of the DCL system was further validated under fault conditions. **Figure 28** presents the scenario of a Single Line to Ground (SLG) fault at Zone 2 km, specifically a Yellow-to-Ground fault. In **Figure 28(a)**, the yellow phase is shorted to ground using a jumper wire. The DCL circuit response is shown in **Figure 28(b)**, where the fault type and location are immediately detected and displayed on the LCD. This information is synchronously logged into the Arduino IoT Cloud, as shown in **Figure 28(c)**. A fault notification is automatically pushed to the responsible engineers' smartphones via the IoT Cloud app (**Figure 28(d)**). The cloud interface also records the associated current spikes for the affected yellow phase and neutral line (**Figure 28(e)**), confirming the SLG condition at Zone 2 km. Additionally, email alerts are dispatched to registered personnel, including a link to the GPS-based Google Maps location of the fault site (**Figure 28(f)**). The link opens directly to a mapped view of the fault location (**Figure 28(g)**), thereby providing actionable information for maintenance teams to respond promptly.

To avoid overwhelming the discussion with an excessive number of figures, this section only presents the results for a representative case: a single line-to-ground (SLG) fault at the yellow phase. In reality, the complete experimental campaign encompassed all 24 distinct fault scenarios, and each scenario was successfully detected, classified, and localized by the proposed system. By focusing on one fault

type in the figures, the paper illustrates the system's capability without redundancy, while still affirming that the method has been comprehensively validated across all tested events.

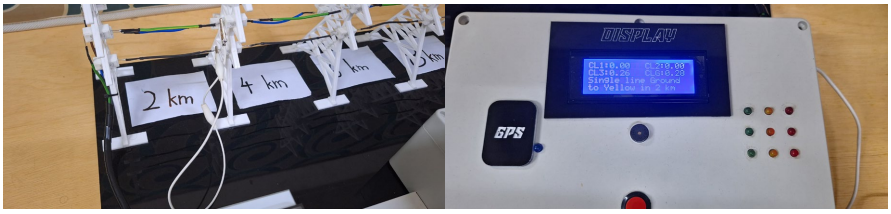

(a) (b)

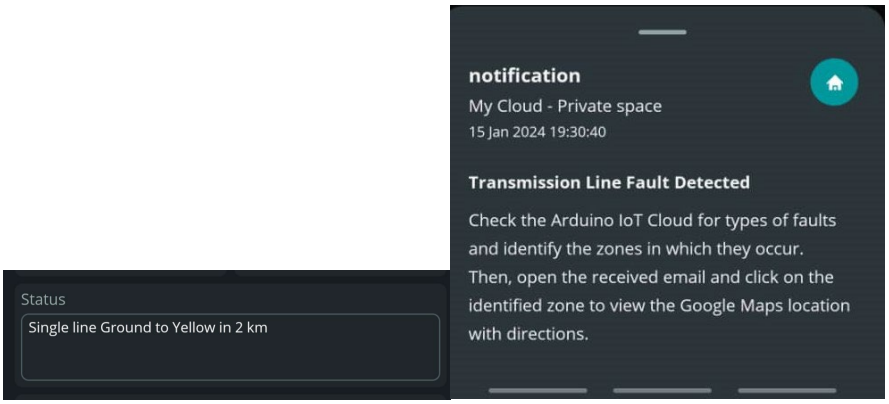

(c) (d)

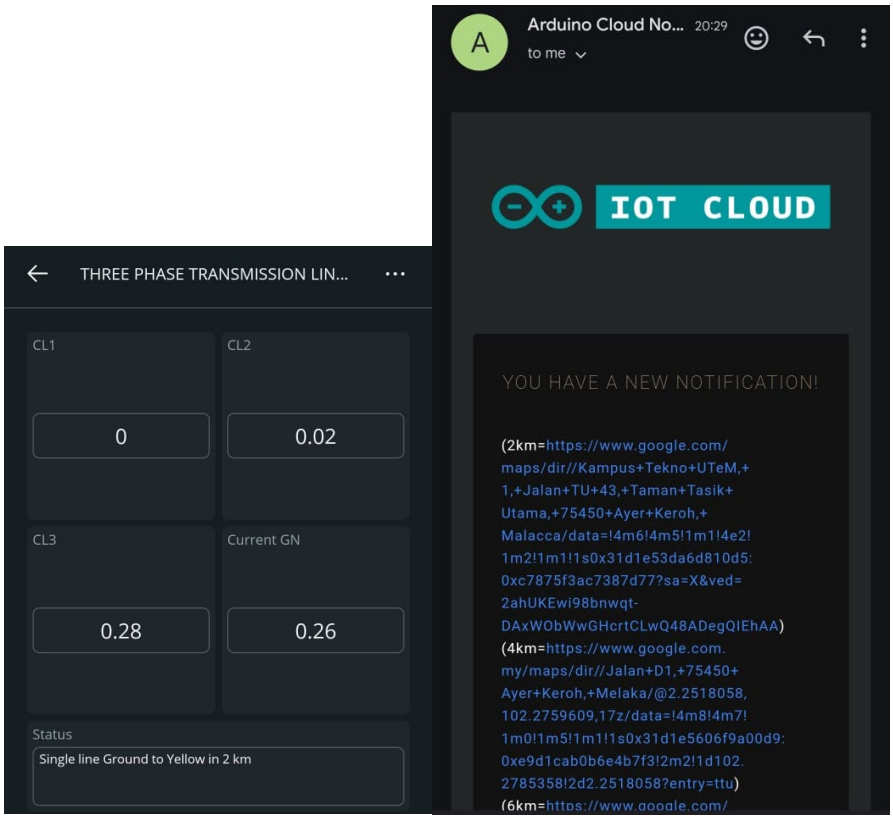

(e) (f)

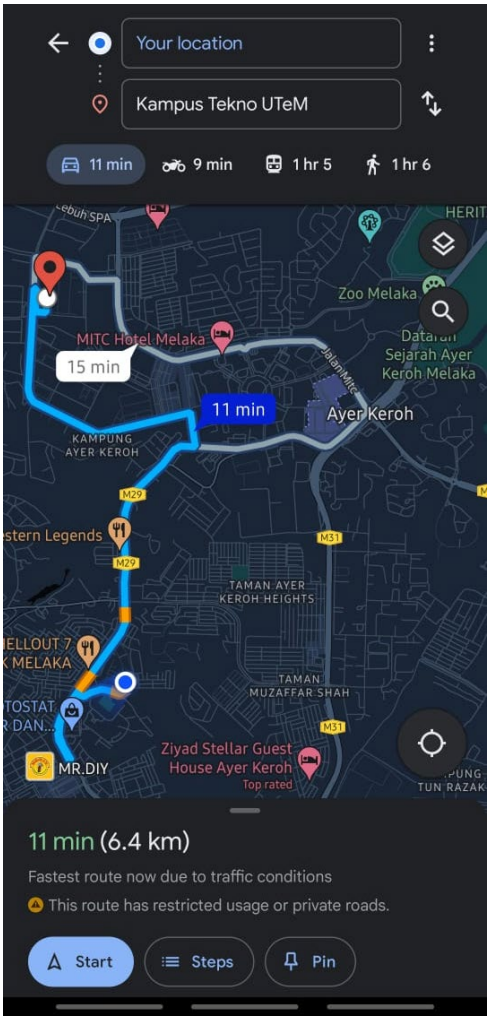

(g)

Figure 28. Fault DCL circuit with SLG (Yellow Phase to Ground) fault established at zone 2 km, (a) Shorting the yellow phase with ground using jumper wire, (b) Fault detection in DCL circuit indicating single line to ground (SLG) Fault at zone 2 km, (c) Single line to ground to yellow in 2 km fault message/notification in Arduino IoT Cloud webpage, (d) Notification received on Engineer's or Person in Charge's Phone via Arduino IoT Cloud phone app, (e) Current values spike for yellow phase and neutral, indicating a single line to ground fault (Yellow Phase to Ground) Detected at 2 km at Arduino IoT Cloud webpage, (f) Tap the received email to open the Google Map location and (g) Displaying the fault location on google maps to help the engineer-in-charge determine the direction.

4.4. Statistical Validation of DCL Performance

A comprehensive statistical analysis was performed to quantitatively validate the robustness and reliability of the proposed fault detection, classification, and localization (DCL) system. Each of the 24 unique fault scenarios (6 fault types across 4 zones) was induced 40 times, resulting in a total of 960 experimental trials. The system demonstrated flawless performance across all trials. The overall accuracy for fault detection, classification, and zone localization was 100%. This performance is summarized in the confusion matrix presented in **Figure 29**.

Actual Fault (Zone) → Predicted Fault (Zone) ↓	RG (2km)	RG (4km)	RG (6km)	RG (8km)	YG (2km)	YG (4km)	YG (6km)	YG (8km)	BG (2km)	BG (4km)	BG (6km)	BG (8km)	RYG (2km)	RYG (4km)	RYG (6km)	RYG (8km)	YBG (2km)	YBG (4km)	YBG (6km)	YBG (8km)	RBG (2km)	RBG (4km)	RBG (6km)	RBG (8km)
RG (2km)	40	0	0	0	0	0	0	0	0	0	0	0	0	0	0	0	0	0	0	0	0	0	0	0
RG (4km)	0	40	0	0	0	0	0	0	0	0	0	0	0	0	0	0	0	0	0	0	0	0	0	0
RG (6km)	0	0	40	0	0	0	0	0	0	0	0	0	0	0	0	0	0	0	0	0	0	0	0	0
RG (8km)	0	0	0	40	0	0	0	0	0	0	0	0	0	0	0	0	0	0	0	0	0	0	0	0
YG (2km)	0	0	0	0	40	0	0	0	0	0	0	0	0	0	0	0	0	0	0	0	0	0	0	0
YG (4km)	0	0	0	0	0	40	0	0	0	0	0	0	0	0	0	0	0	0	0	0	0	0	0	0
YG (6km)	0	0	0	0	0	0	40	0	0	0	0	0	0	0	0	0	0	0	0	0	0	0	0	0
YG (8km)	0	0	0	0	0	0	0	40	0	0	0	0	0	0	0	0	0	0	0	0	0	0	0	0
BG (2km)	0	0	0	0	0	0	0	0	40	0	0	0	0	0	0	0	0	0	0	0	0	0	0	0
BG (4km)	0	0	0	0	0	0	0	0	0	40	0	0	0	0	0	0	0	0	0	0	0	0	0	0
BG (6km)	0	0	0	0	0	0	0	0	0	0	40	0	0	0	0	0	0	0	0	0	0	0	0	0
BG (8km)	0	0	0	0	0	0	0	0	0	0	0	40	0	0	0	0	0	0	0	0	0	0	0	0
RYG (2km)	0	0	0	0	0	0	0	0	0	0	0	0	40	0	0	0	0	0	0	0	0	0	0	0
RYG (4km)	0	0	0	0	0	0	0	0	0	0	0	0	0	40	0	0	0	0	0	0	0	0	0	0
RYG (6km)	0	0	0	0	0	0	0	0	0	0	0	0	0	0	40	0	0	0	0	0	0	0	0	0
RYG (8km)	0	0	0	0	0	0	0	0	0	0	0	0	0	0	0	40	0	0	0	0	0	0	0	0
YBG (2km)	0	0	0	0	0	0	0	0	0	0	0	0	0	0	0	0	40	0	0	0	0	0	0	0
YBG (4km)	0	0	0	0	0	0	0	0	0	0	0	0	0	0	0	0	0	40	0	0	0	0	0	0
YBG (6km)	0	0	0	0	0	0	0	0	0	0	0	0	0	0	0	0	0	0	40	0	0	0	0	0
YBG (8km)	0	0	0	0	0	0	0	0	0	0	0	0	0	0	0	0	0	0	0	40	0	0	0	0
RBG (2km)	0	0	0	0	0	0	0	0	0	0	0	0	0	0	0	0	0	0	0	0	40	0	0	0
RBG (4km)	0	0	0	0	0	0	0	0	0	0	0	0	0	0	0	0	0	0	0	0	0	40	0	0
RBG (6km)	0	0	0	0	0	0	0	0	0	0	0	0	0	0	0	0	0	0	0	0	0	0	40	0
RBG (8km)	0	0	0	0	0	0	0	0	0	0	0	0	0	0	0	0	0	0	0	0	0	0	0	40

Abbreviations: SLG: Single Line to Ground (R: Red, Y: Yellow, B: Blue); DLG: Double Line to Ground (RY: Red-Yellow, YB: Yellow-Blue, RB: Red-Blue).

Figure 29. Confusion matrix summarizing DCL system performance (Total Trials: 960).

The confusion matrix is structured such that the rows represent the Actual Fault that was induced, and the columns represent the Predicted Fault as identified by the system. The diagonal cells (shaded green) show the number of correct classifications for each fault type and zone. The off-diagonal elements would indicate misclassifications; however, all are zero, confirming that no misdetections or misclassifications occurred. This perfect classification rate confirms the efficacy of the threshold-based algorithm running on the ESP32 and the reliability of the hardware setup for the tested SLG and DLG fault conditions.

5. Conclusion

This study successfully designed and implemented a Wi-Fi and GPS-based smart monitoring system for fault detection, classification, and localization (DCL) in three-phase transmission lines using Arduino and IoT technologies. The system demonstrated 100% accuracy across 24 fault scenarios (SLG and DLG types across four distance zones) through 960 experimental trials. The integration of ACS712 sensors, Arduino Mega, ESP32, and GPS enabled real-time data acquisition, cloud-based monitoring, and precise fault localization with an error margin of ±5 meters. The proposed system addresses key limitations of prior works, including a lack of cloud integration, limited fault types, and the absence of GPS-based localization. It offers a cost-effective, scalable, and real-time solution for enhancing grid reliability and reducing outage times. The current prototype uses a single-phase emulation of three-phase behaviour, which may not fully capture all transient behaviours of a true three-phase system. Future work will include full three-phase implementation, integration of machine learning for predictive maintenance, and enhanced cybersecurity measures for IoT communication.

Acknowledgements

This research work is funded by the Ministry of Higher Education (MoHE) of Malaysia through the Centre for Research and Innovation Management UTeM

Publication Initiative 2025. The authors would also like to thank Universiti Teknikal Malaysia Melaka (UTeM), thanks for all the support.

Conflicts of Interest

The authors declare no conflicts of interest regarding the publication of this paper.

References

[1] Uddin, M.S., Hossain, M.Z., Fahim, S.R., Sarker, S.K., Bhuiyan, E.A., Muyeen, S.M., *et al.* (2022) On the Protection of Power System: Transmission Line Fault Analysis Based on an Optimal Machine Learning Approach. *Energy Reports*, **8**, 10168-10182. https://doi.org/10.1016/j.egyr.2022.07.163

[2] Zheng, T., Liu, M., Puthal, D., Yi, P., Wu, Y. and He, X. (2022) Smart Grid: Cyber Attacks, Critical Defense Approaches, and Digital Twin. https://arxiv.org/pdf/2205.11783

[3] Asman, S.H., Ab Aziz, N.F., Ungku Amirulddin, U.A. and Ab Kadir, M.Z.A. (2021) Transient Fault Detection and Location in Power Distribution Network: A Review of Current Practices and Challenges in Malaysia. *Energies*, **14**, Article 2988. https://doi.org/10.3390/en14112988

[4] Ferreira, E.F. and Barros, J.D. (2018) Faults Monitoring System in the Electric Power Grid of Medium Voltage. *Procedia Computer Science*, **130**, 696-703. https://doi.org/10.1016/j.procs.2018.04.123

[5] Trindade, F.C.L. and Freitas, W. (2017) Low Voltage Zones to Support Fault Location in Distribution Systems with Smart Meters. *IEEE Transactions on Smart Grid*, **8**, 2765-2774. https://doi.org/10.1109/tsg.2016.2538268

[6] Naidu, O.D. and Pradhan, A.K. (2021) Precise Traveling Wave-Based Transmission Line Fault Location Method Using Single-Ended Data. *IEEE Transactions on Industrial Informatics*, **17**, 5197-5207. https://doi.org/10.1109/tii.2020.3027584

[7] Alam, M.N., Hasan Buiyan, M.Z., Al Hasan Anik, M.A., Tanvir, F. and Fahim, T.A. (2024) Enhancing Power Grid Reliability in Bangladesh: An IoT-Based Approach to Transmission Line Fault Detection. 2024 *IEEE 3rd International Conference on Robotics, Automation, Artificial-Intelligence and Internet-of-Things* (*RAAICON*), Dhaka, 9-30 November 2024, 224-229. https://doi.org/10.1109/raaicon64172.2024.10928383

[8] S, A., A, A.G., Kumar M, A. and S, P.M. (2020) Transmission Lines Management System for Smart Grids. 2020 *IEEE International Women in Engineering* (*WIE*) *Conference on Electrical and Computer Engineering* (*WIECON-ECE*), Bhubaneswar, 26-27 December 2020, 44-47. https://doi.org/10.1109/wiecon-ece52138.2020.9397962

[9] Al Mtawa, Y., Haque, A. and Halabi, T. (2022) A Review and Taxonomy on Fault Analysis in Transmission Power Systems. *Computation*, **10**, Article 144. https://doi.org/10.3390/computation10090144

[10] Mukherjee, A., Kundu, P.K. and Das, A. (2021) Transmission Line Faults in Power System and the Different Algorithms for Identification, Classification and Localization: A Brief Review of Methods. *Journal of The Institution of Engineers* (*India*): *Series B*, **102**, 855-877. https://doi.org/10.1007/s40031-020-00530-0

[11] Rathod, S., Ghar, A., Palve, P., Patil, M. and Khadse, V. (2022) Fault Detection in Transmission Line Using Arduino Uno. International Research *Journal of Mod-Ernzation in Engineering Technology and Science*, **4**, 1860-1862.

https://www.irjmets.com/paperdetail.php?paperId=15da6d2fc55ede05107c2b9bb10a4230

[12] Saravanan, S., Sameer, M., Deekshith, N., Parthasardhi, P., Kumar, D.G. and Prameela, M. (2023) Identification and Detection of Fault in Distribution System Using Arduino Uno. 2023 2*nd International Conference on Edge Computing and Applications* (*ICECAA*), Namakkal, 19-21 July 2023, 1223-1226. https://doi.org/10.1109/icecaa58104.2023.10212326

[13] Nianga-Apila, M., Gogom, A., Ganongo, A.O., Gomba, R. and Ganga, G. (2025) Detecting and Locating Short-Circuit Faults in Electrical Mesh Networks. *Energy and Power Engineering*, **17**, 134-153. https://doi.org/10.4236/epe.2025.176007

[14] Gautam, M.K., Kumar, P., Prasad, D., Gupta, P. and Yadav, K.P. (2025) Real-Time Detection and Classification of Three-Phase Transmission Line Faults Using an IoT-Enabled Arduino and ESP32 Embedded System. *International Journal of Advanced Research in Science*, *Communication and Technology*, **5**, 425-431.

[15] Kumar, A. (2024) Three Phase Transmission Line Fault Detection Using Arduino. *International Journal for Research in Applied Science and Engineering Technology*, **12**, 4169-4183. https://doi.org/10.22214/ijraset.2024.62482

[16] Dhoke, G., Dhurve, A., Pandagre, A., Farkade, S. and Sune, M. (2025) Design and Implementation of a Three Phase Transmission Line Fault Detection and Protection using Arduino. *International Journal on Science and Technology* (*IJSAT*), **16**, 1-9.

[17] Mehdi, A., Kim, C., Hussain, A., Kim, J. and Hassan, S.J.U. (2021) A Comprehensive Review of Auto-Reclosing Schemes in AC, DC, and Hybrid (AC/DC) Transmission Lines. *IEEE Access*, **9**, 74325-74342. https://doi.org/10.1109/access.2021.3077938

[18] Qiao, Z. and Fan, W. (2013) Identification of Permanent Faults for Three-Phase Autoreclosing Using Inductance Parameter on Transmission Lines with Shunt Reactors. *International Journal of Smart Home*, **7**, 197-206. https://doi.org/10.14257/ijsh.2013.7.5.20

[19] Blumschein, J., Yelgin, Y. and Ludwig, A. (2017) Adaptive Autoreclosure to Increase System Stability and Reduce Stress to Circuit Breakers. 2017 70*th Annual Conference for Protective Relay Engineers* (*CPRE*), College Station, 3-6 April 2017, 1-8. https://doi.org/10.1109/cpre.2017.8090004

[20] Tharma Raja, S.R. (2024) Design of Wi-Fi and GPS-Based Smart Monitoring and Fault Detection System for Three-Phase Power Transmission Line Using Arduino. Bachelor's Thesis, Universiti Teknikal Malaysia Melaka.